J. Phys. D: Appl. Phys. **29** (1996) 1779–1798. Printed in the UK

Direct experimental determination of the atomic structure at internal interfaces

N D Browning† and S J Pennycook‡

† Department of Physics (M/C 273), University of Illinois at Chicago, 845 West Taylor Street, Chicago, IL 60607-7059, USA
‡ Solid State Division, Oak Ridge National Laboratory, PO Box 2008, Oak Ridge, TN 37831-6030, USA

Received 14 August 1995, in final form 16 January 1996

Abstract. A crucial first step in understanding the effect that internal interfaces have on the properties of materials is the ability to determine the atomic structure at the interface. Because interfaces can contain atomic disorder, dislocations, segregated impurities and interphases, sensitivity to all of these features is essential for complete experimental characterization. By combining *Z*-contrast imaging and electron energy loss spectroscopy (EELS) in a dedicated scanning transmission electron microscope (STEM), the ability to probe the structure, bonding and composition at interfaces with the necessary atomic resolution has been obtained. Experimental conditions can be controlled to provide, simultaneously, both incoherent imaging *and* spectroscopy. This enables interface structures observed in the image to be interpreted intuitively and the bonding in a specified atomic column to be probed directly by EELS. The bonding and structure information can then be correlated using bond-valence sum analysis to produce structural models. This technique is demonstrated for 25°, 36° and 67° symmetric and 45° and 25° asymmetric [001] tilt grain boundaries in $SrTiO_3$. The structures of both types of boundary were found to contain partially occupied columns in the boundary plane. From these experimental results, a series of structural units were identified which could be combined, using continuity of grain boundary structure principles, to construct all [001] tilt boundaries in $SrTiO_3$. Using these models, the ability of this technique to address the issues of vacancies and dopant segregation at grain boundaries in electroceramics is discussed.

1. Introduction

Internal interfaces are known to play a dominant role in determining the overall bulk mechanical and electrical characteristics of many materials. The framework around which any understanding of this role must be built is a knowledge of the atomic structure and any change in composition and bonding, relative to the bulk, that occurs at the interface. There are various techniques in transmission electron microscopy to study these atomic scale effects at interfaces experimentally. Both conventional transmission electron microscopes (TEM) [1–4] and scanning transmission electron microscopes (STEM) [5, 6] provide the capability of imaging interface structures on the atomic scale. Using a spectrometer to filter the scattered electrons by energy loss, composition changes can also be imaged on the nanometre scale [7–9]. Additionally, recent developments in detection schemes [10, 11] for dedicated electron energy loss spectroscopy (EELS) have permitted bonding and composition fluctuations to be measured on the atomic scale [12, 13].

In characterizing interfaces it is useful to classify them into one of two groups; homophase (grain boundaries in single-phase materials) and heterophase (composite interfaces such as metal–ceramic interfaces). In addition, in each of these groups the interface can be clean, have segregated impurities or contain a different phase from the bulk (interphase). Characterization of these interfaces presents a range of experimental problems. For instance, heterophase interfaces and homophase boundaries with high segregant concentrations and large interphases (more than one unit cell) represent relatively straightforward systems to characterize. Distinct composition changes at these interfaces can be mapped with sub-nanometre spatial resolution utilizing EELS [14–16]. Composition changes can be correlated with high-resolution TEM images [17, 18] to determine a composition gradient and width of the interface, which in turn can be related phenomenologically to the macroscopic properties of the material. Although such spatial resolution is often sufficient for these interfaces, at the other end of the characterization scale are clean homophase boundaries and homophase

 © 1996 IOP Publishing Ltd

and heterophase interfaces with low concentrations of segregants and small interphases. These types of interface can also have a profound effect on the properties of materials, yet changes in composition, bonding and structure can be very subtle. These changes can occur abruptly at the interface [12] or occur gradually over a few unit cells either side of the interface [5]. It is therefore essential to be able to observe the atomic structure at interfaces *and* know the exact crystallographic location from which an energy loss spectrum is acquired in order to characterize the whole range of interfaces that are of importance for materials science fully.

In this paper a direct experimental technique for obtaining the atomic structure at internal interfaces is presented. This technique utilizes the unique capabilities of the dedicated STEM to obtain simultaneous, incoherent, atomic-resolution Z-contrast images and energy loss spectra. This detection scheme has the advantage that the Z-contrast image can be used to position the electron probe accurately over an individual atom column or plane [12, 13]. The energy loss spectrum that is obtained can therefore be related to a known atomic location, permitting the bonding and composition information in the spectrum to be correlated with the atomic structure. The sensitivity of the Z-contrast image to heavier elements, coupled with the highest EELS cross sections for elements of low atomic number, means that these two techniques can provide complementary information on multicomponent compounds. This information is combined by means of bond-valence-sum analysis [20, 21] to produce structural models for interfaces.

The use of this technique is illustrated by the study of clean homophase [001] tilt grain boundaries in $SrTiO_3$. Experimental results have been obtained from 25°, 36° and 67° symmetric and 45° and 25° asymmetric grain boundaries in commercially produced bicrystals. All of these structures were found to contain partially occupied columns in the boundary plane. Additionally, a series of structural units were identified from the experimental results which could be combined using the principles of continuity of grain boundary structure [22, 23] to predict all other [001] tilt boundaries in $SrTiO_3$. These boundary structures illustrate the variation in atomic structure that exists along homophase grain boundaries and highlight potential locations for the incorporation of dopant atoms.

2. Experimental techniques

The electron optics in the dedicated STEM are designed to produce a beam of electrons that illuminates a small area on the surface of the specimen. Typically this 'spot size' or 'electron probe' is 2.2 Å FWHM for the VG HB501 STEM operating at 100 kV. An image is formed by rastering the probe over the surface of the specimen and collecting the transmitted electrons in a variety of detectors (figure 1). The integrated output from these detectors is then displayed on a TV screen scanning at the same rate as the probe.

For crystalline specimens aligned in zone-axis orientations, it has been noticed that the coherent STEM probe forms narrow spikes around the atomic columns [24, 25].

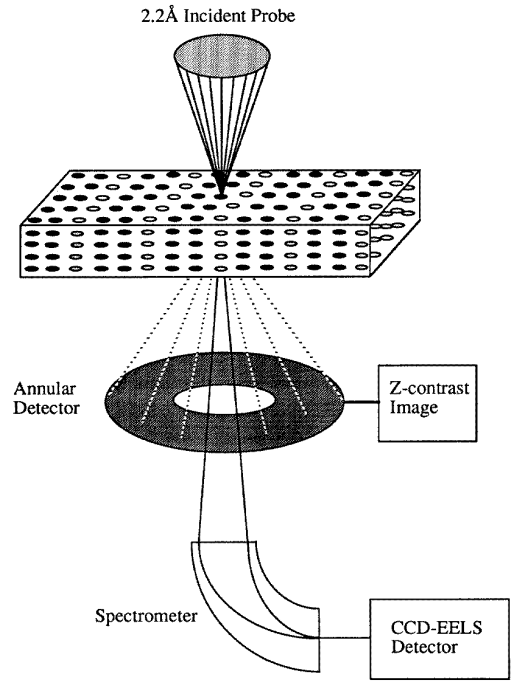

Figure 1. A schematic diagram of the detector arrangement in the VG HB501 dedicated STEM showing that the atomic resolution Z-contrast image and the atomic-resolution electron energy loss spectrum can be acquired simultaneously.

An alternative to calculating the intensity of the probe as it penetrates the specimen using multi-slice calculations [26, 27] can be obtained using the Bloch wave description of the propagation of a coherent incident probe through the specimen [28, 29]. In this description, the Bloch states resemble molecular orbitals for axial illumination and can be assigned s-type and p-type natures. Integration over the coherent incident probe causes the s-type states to add constructively while the p-type states interfere destructively, with the net effect being the channelling of the probe down the atomic columns. Therefore, if the atomic column spacing is larger than the 2.2 Å probe size, an atomic column can be illuminated individually on the surface of the specimen and this individual column illumination is maintained through the specimen. In thicker specimens, in which dynamical diffraction effects would be expected to broaden the probe significantly, the channelling effect preserves the high spatial resolution of the signal. However, in thick specimens there is absorption of the s states, analogous to depletion of the incident beam by scattering, that causes the contrast to diminish with thickness.

Electrons scattered out of this incident beam are typically collected in two imaging detectors, bright-field and dark-field ones (figure 1). The bright-field detector collects the small-angle scattering and produces an image similar to that of a conventional TEM, whereas the dark-field detector collects electrons scattered in the range 40–150 mrad for which the dominant contribution to the scattered intensity is thermal diffuse scattering [28, 29]. The large angular range of this detector averages

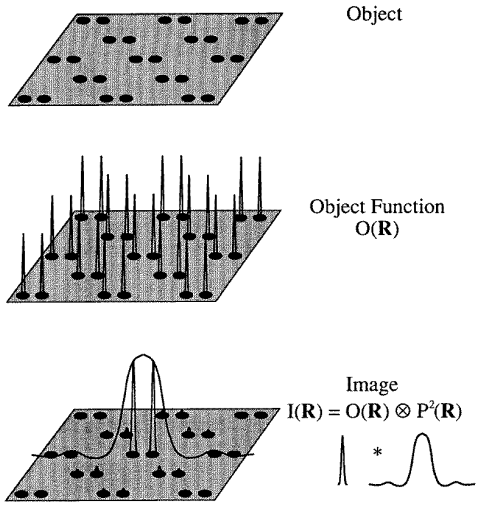

Figure 2. Associated with a specimen in a zone-axis orientation (*a*) is an object function for each column (*b*) which describes the probability of scattering to the high-angle detector. The experimental Z-contrast image (*c*) is obtained from a convolution of this object function with the probe intensity profile.

any transverse coherence effects between neighbouring columns. This transverse incoherence results in a straightforward interpretation of the image, with a 'bright spot' corresponding to an atomic column. Interpretation of the intensity of the atomic columns, however, is not so simple, because the detector geometry does not destroy coherent effects between atoms in the atomic column, namely parallel to the beam direction. To understand how this coherence affects the image, the nature of thermal diffuse scattering must be considered.

Thermal diffuse scattering has traditionally been described by the Einstein model [30, 31], whereby each atom is considered to be an independent source of thermal diffuse scattering. For this purely incoherent model, the scattered intensity into the dark-field detector approximates to the Z^2-dependence of the Rutherford scattering cross section. However. a more precise model for thermal diffuse scattering has been developed by Jesson and Pennycook, based on the work of Warren [32], that includes all orders of phonon scattering [33]. Here, coherent effects are found to be important for two or three neighbouring atoms along a column. For columns shorter than this, coherent effects dominate the image, but for longer columns, the Z^2-dependence in the Einstein model is only modulated by the residual correlations in the two or three atom packets. These residual correlations only become important in cases in which the atomic spacing is different in adjacent columns, because, for two dissimilar species columns of the same spacing, the correlations simply provide an overall scaling of the image intensity. To a good approximation, therefore, the Z-contrast image can be considered to be incoherent, with the dominant factor controlling image intensity being the atomic number of the elements present in the specimen.

For the high-angle signal, the specimen can therefore be considered to consist of an array of independently scattering atomic columns (figure 2(*a*)). Associated with each of these atomic columns is a probability of a scattered electron reaching the detector, or scattering power (figure 2(*b*)). The resultant image created as the probe is scanned across the surface of the specimen, can be described by a simple

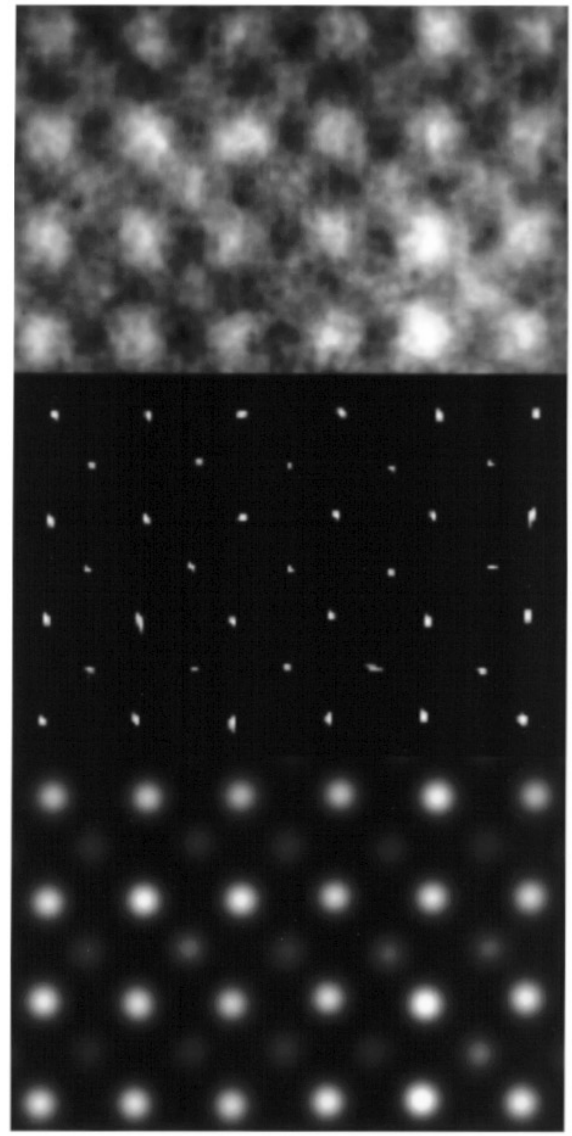

Figure 3. (*a*) A Z-contrast image of [001] $SrTiO_3$ which has a cubic perovskite structure (space group *Pm*3*m*) with a lattice parameter of 3.905 Å. In the [001] projection, the titanium–strontium spacing is 2.76 Å which is within the resolution limits of the 2.2 Å probe of the 100 kV VG HB501 UX STEM. Z-contrast images of $SrTiO_3$ in this projection therefore show columns containing strontium (Z = 38) or titanium (Z = 22) which can be identified by their relative intensities (the titanium column is in reality alternating atoms of oxygen and titanium through the thickness of the sample and the column intensity is roughly proportional to $Z_{Ti}^2 + Z_O^2$). Columns consisting of entirely oxygen atoms (Z = 8) are not observed in this detection scheme. (*b*) The maximum entropy processing reduces the image to an array of points which can be re-convoluted with the probe for ease of viewing (*c*). The contrast in the original image is preserved in the maximum entropy object function.

convolution of the probe intensity profile with an object function for the scattering power from the columns into the dark-field detector (figure 2(*c*)):

$$I(\boldsymbol{R}, t) = O(\boldsymbol{R}, t) \otimes P_{eff}^2(\boldsymbol{R}). \quad (1)$$

This incoherent image formalization allows the maximum entropy image processing technique to be used to recover the object functions [34, 35]. Maximum entropy is a statistical technique, based on Bayesian probability theory, that is designed to produce the object function which, when convoluted with the microscope probe, gives the best fit to the experimental image. An example of the processing technique applied to $SrTiO_3$ is shown in figure 3. The technique makes no assumptions in generating the object function and starts from an object function of uniform intensity. The accuracy of this technique is limited by the statistics of the image and local tilting effects which invariable occur at interfaces in real specimens. These effects lead to a blurring and distortion of the positions of the atomic columns. To ensure that the program is not generating atomic columns in the object function, it is always compared to the original image. From studies of perfect crystals it is expected that the atomic column positions can be determined to within an accuracy of about 0.2 Å [36, 37].

Although this technique can determine the atomic column positions to high accuracy, the coherent effects along the atomic columns still prevent accurate compositional quantification. From the image shown in figure 3 it can be seen that the contrast between the strontium (Sr) columns ($Z = 38$) and the titanium–oxygen (Ti–O) columns (intensity roughly proportional to $Z_{\mathrm{Ti}}^2 + Z_{\mathrm{O}}^2$) is preserved in the maximum entropy object function (the Sr columns are all brighter than the Ti–O columns). However, at interfaces, where vacancies and defects are more prevalent, the distinctions between neighbouring atomic columns of different composition are less clear. As well as the previously mentioned problems, other second-order effects such as a change in the atomic vibration amplitude for atoms in the interface plane, disorder scattering and dechannelling due to surface relaxation of strained regions near the interface can all affect the scattering power of the column. To characterize interfaces further it is necessary to combine Z-contrast imaging with other experimental techniques such as EELS.

As can be seen from figure 1, the Z-contrast detector does not interfere with the low-angle scattered electrons used for electron energy loss spectroscopy (EELS). The Z-contrast image can therefore be used to position the probe for EELS to be obtained from individual atomic columns. Energy loss spectroscopy has two traditional uses in micro-analysis [38]. The integrated intensity in the characteristic energy loss edges is proportional to the number of atoms present, allowing detailed compositional analysis to be performed. However, arguably the most important feature of the energy loss spectrum for interface analysis is its sensitivity to local electronic structure. Changes in coordination and oxidation state are known to have strong effects on the shapes of core edges [39–42]. This means that, when combined with the Z-contrast image, the structure at an interface can be directly correlated with the local electronic environment and hence the bonding, on the atomic scale.

For complete correlation between the spectroscopy and the structural image on the atomic scale it is necessary for the inelastic image to have the same incoherent form, namely an object function peaked on the atomic columns. Then, provided that the localization of the energy loss process is smaller than the interatomic spacing of the material under study, beam channelling will again occur and atomic resolution spectra can be obtained from relatively thick specimens. The optical equation for incoherent imaging with inelastically scattered electrons has been derived by Ritchie and Howie [43]. The derivation follows similar lines to that for elastic scattering [33] and gives an image intensity, when all scattered electrons are collected, which can be written in the same form as equation (1), but now with an inelastic object function $O'(\boldsymbol{R})$ [44–46]:

$$I(\boldsymbol{R}, t) = O'(\boldsymbol{R}, t) \otimes P_{eff}^2(\boldsymbol{R}). \quad (2)$$

Ritchie and Howie showed that the matrix elements in this inelastic object function may be calculated in the semi-classical approximation, namely assuming no deflection of the fast electron trajectory, which was convenient for their study of the excitation of surface plasmons. For elemental quantification and ease of interpretation of spectral features, the core-loss region of the spectrum represents a more attractive area of study for the majority of materials applications. In this case, the hydrogenic model developed by Maslen, Allen and Rossouw for the object function is more appropriate [47–51]. Object functions calculated using this hydrogenic model show that, for all K shells within the range 0–2 kV (namely those of Si, O, C, Be and Li) the FWHM is less than 1 Å [46], implying that atomic resolution is achievable. Recent calculations for L edges have shown that this signal is also localized at the atom cores [52], with characteristic losses as low as 190 eV having a FWHM less than 1 Å. For the cobalt L edge, the predicted localization is in good agreement with the 86–87% drop in intensity observed in moving a single plane across a $CoSi_2$–Si (111) interface [12]. As a general rule, atomic resolution spectroscopy is most favourable for light elements, for which the edge occurs well into the core-loss region of the spectrum (> 200 eV). For this energy range, the ability to obtain atomic resolution spectra is indicated simply by the ability to obtain an atomic-resolution image.

Using the Z-contrast image to position the probe for energy loss spectroscopy has certain advantages for crystalline materials. The Z-contrast image is much more intense than a core-loss energy filtered image or spectrum image [7–9], allowing exposure times to be kept to a minimum and greatly reducing the number of spectra. Additionally, it is well known that spectroscopy from crystalline materials in zone-axis orientations can lead to quantitation errors [53]. However, if the probe is placed in the same crystallographic location, say in exactly one unit cell steps across the interface, these errors are eliminated. A linescan across a crystalline interface that does not position the probe in increments of the atomic column spacing will result in different channelling conditions and

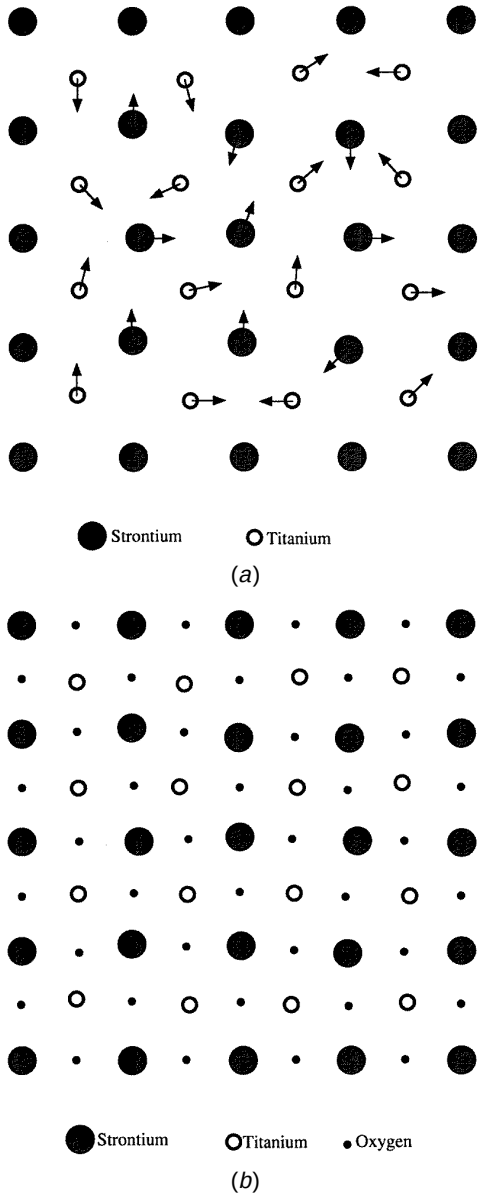

Figure 4. (*a*) A schematic diagram of a Z-contrast image of the [001] projection of a 4×4 unit cell block of $SrTiO_3$, with outer atoms in the block in the expected lattice sites and the atoms inside displaced from their lattice positions by an average of 0.2 Å (consistent with the error expected from the maximum entropy technique). The arrows represent the direction of displacement with size proportional to displacement. (*b*) The structure obtained when the oxygen atoms are placed consistent with the knowledge of the bulk structure (Sr = $+2.13 \pm 0.12$, Ti = $+4.27 \pm 0.35$ and O = -2.13 ± 0.27). (*c*) The bond-valence-sum-minimized structure (Sr = $+2.13 \pm 0.04$, Ti = $+4.15 \pm 0.03$ and O = -2.09 ± 0.02). Again the sizes of the arrows represent the displacements relative to the perfect lattice, on the same scale as in (*a*). The atoms without arrows are within 0.05 Å of the perfect lattice sites.

hence quantitation errors. Another advantage is that the Z-contrast image can be used to locate likely dopant or segregant sites. Focusing the beam down to an individual column in principle enables very small doping levels to be

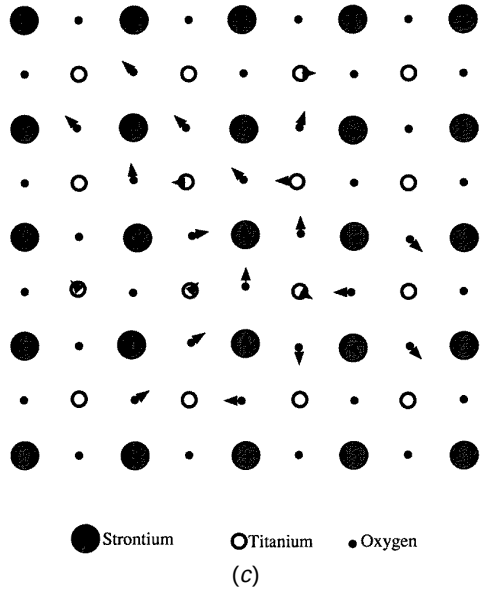

Figure 4. (Continued.)

observed because the area being probed by the beam is only one atom wide and about 50–100 atoms thick [54].

The Z-contrast image can also be used as a monitor for beam damage and surface damage caused during the thinning process. Because the Z-contrast image is controlled by the probe at the surface of the specimen, to obtain an image the surface must be clean and crystalline. This is of crucial importance for the study of interfaces where fine structure changes in the energy loss spectrum will be shielded by surface layers. Because interfaces tend to mill faster than the bulk, performing composition profile measurements without knowing the structure at the interface can lead to results which may be an indication of the decomposition profile of the interface rather than representative of the bulk. Interfaces can also be subject to density changes relative to the bulk which can affect the background of the edge under study. By using the Z-contrast image to determine the structure, the spectrum can be used to determine changes in bonding and coordination. This eliminates the need to quantify the energy loss spectrum and thus eliminates the problems associated with density changes.

3. Bond-valence structural models

Having defined a technique for obtaining the structure, composition and bonding at an interface on the atomic scale, the question becomes how to combine the two sets of data to produce a structural model. For reasons mentioned in the previous section, quantification both of the image and of the energy loss spectrum to measure differences in atomic concentrations of the order of a few atoms is beyond the detection limits of current microscopes. However, the Z-contrast image does give the heavy-element column positions to within an accuracy of about 0.2 Å and the energy loss spectrum gives information on the coordination

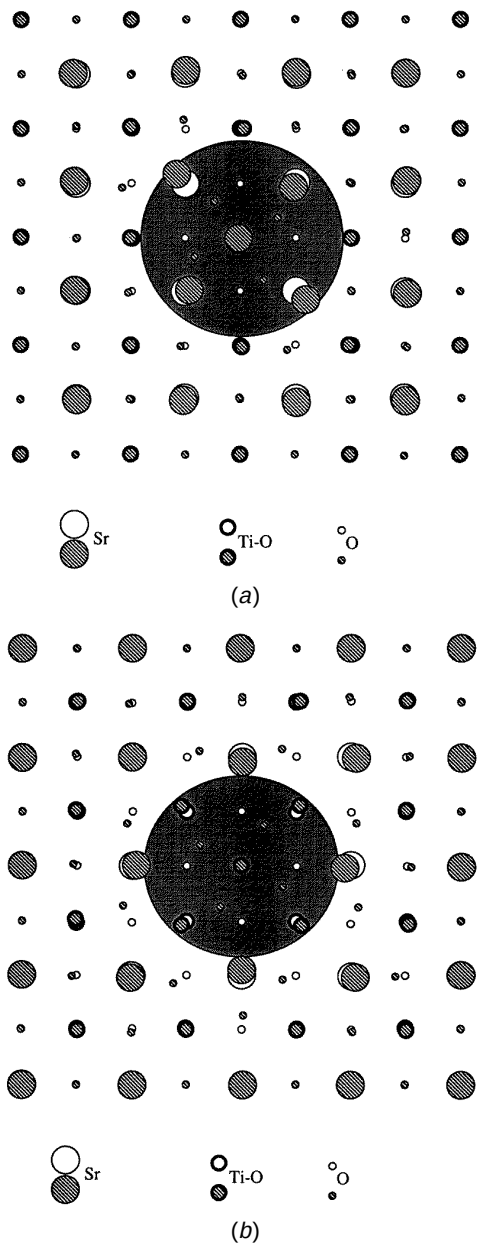

Figure 5. (*a*) The bond-valence-sum-minimized structure with one of the titanium columns mistakenly identified as strontium (Sr = +2.27 ± 0.19, Ti = +4.15 ± 0.04 and O = −2.08 ± 0.08). The surrounding columns outside the circle marked in the figure are relatively unaffected (positions are still within 0.1 Å of lattice sites and valences are still within ±0.1). For the columns within the circle, the distortions in valences become greater (+1) towards the centre of the circle, pointing to the offending atomic column. (*b*) The bond-valence-sum minimization for a structure in which one strontium atom is mistakenly identified as titanium.

of the light elements surrounding these columns. Using the image of the heavy elements as a base model, the light elements can be arranged to obtain a structural model consistent with the energy loss spectrum. To do this on a quantitative basis, bond-valence-sum calculations can be used [20, 21].

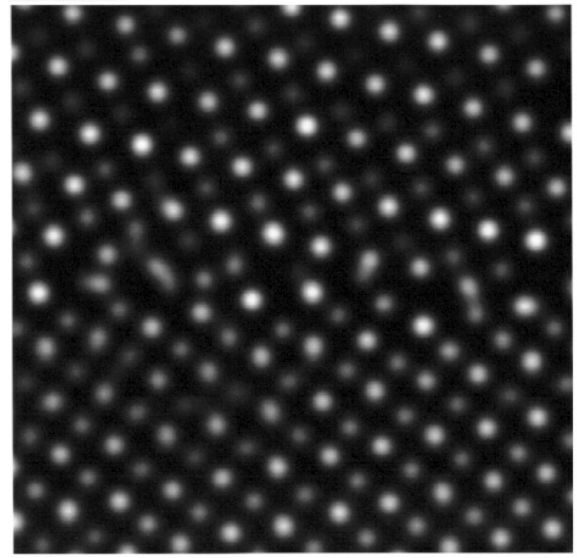

Figure 6. The maximum entropy object function for the 25° (920) [001] tilt grain boundary in $SrTiO_3$.

Bond-valence-sum calculations utilize a concept proposed by Pauling [55] in which a fraction of the formal valence of an atom can be assigned to each of its bonds. The contribution of each of these individual bonds, S, to the formal valence of the atoms involved in the bond is governed by the bond length through the expression

$$S = \exp[(r_0 - r_{ij})/B] \tag{3}$$

where r_0 is a constant characteristic of the elements in the bond, B is a constant which has been assigned the value 0.37 by fitting to experimental data from a wide range of materials and r_{ij} is the bond length [20, 21].

It should be noted, as has been pointed out by Jansen and Block [56], that bond-valence sums are empirical calculations that can be derived from the Born–Mayer model for ionic solids and are only accurate to within about 10% inaccuracy. Additionally, their use is only strictly valid for perfect crystal structures. However, for electron microscopy applications, the atom column positions can only be determined to within about 0.2 Å, making the errors in the bond-valence calculations a second-order effect. As such, the main use of bond-valence-sum calculations in this paper is to validate interface structures by eliminating any structure in which there are significant deviations from the expected formal valence. Such a formalization does not attempt to predict a minimum energy structure for an interface, but shows that the atom positions determined by Z-contrast and the light elements positioned in accordance with the EELS spectra do not violate crystal chemistry principles.

As an example of the type of problem that can be investigated by bond-valence-sum calculations, shown in figure 4(*a*) is a schematic diagram of that which may be observed in the Z-contrast image of the [001] projection of a 4 × 4 unit cell block of $SrTiO_3$. The outer atoms in the block are in the expected lattice sites ($SrTiO_3$ has a cubic perovskite structure (space group $Pm3m$) with

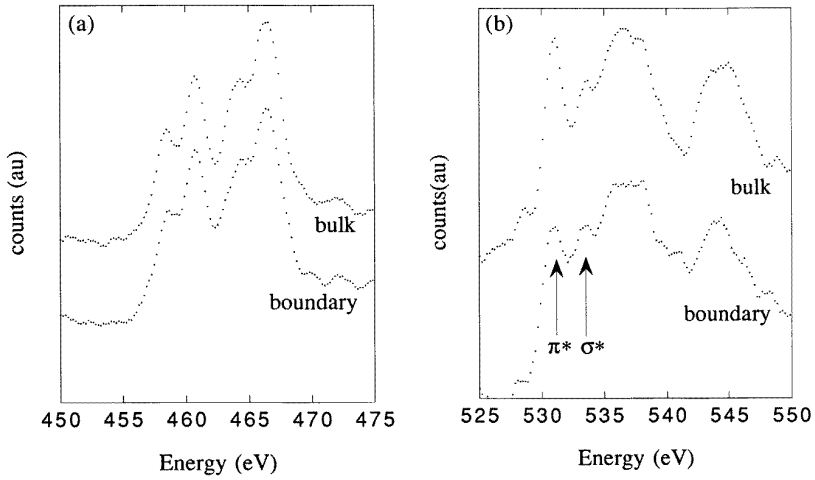

Figure 7. Titanium L edge spectra from the bulk and boundary (*a*) reveal substantially no change in the overall edge intensity, L_2/L_3 ratio or edge-onset position, indicating no change in the overall formal valence of the titanium atoms at the boundary. Oxygen K edge spectra from the bulk and boundary (*b*) show only a change in the relative intensity of the π^* and σ^* peaks, indicating that the octahedral coordination of the oxygen atoms at the boundary is maintained and that there is a slight disruption of the linear Ti–O bonds at the boundary itself.

a lattice parameter of 3.905 Å), but the atoms inside are displaced from their lattice positions by an average of 0.2 Å (consistent with the error expected from the maximum entropy technique). Using our knowledge of the perfect crystal structure, oxygen atoms can be placed in positions between the metal atom columns (remembering that this is a 2D projection of a 3D structure and that the oxygen atoms are on the same plane as the titanium atoms, separated by 1.9525 Å in the [001] direction from the plane containing strontium). The average valences and the standard deviation from the expected value of the atoms in the structure can be calculated using equation (3). For the structure in figure 4(*b*) these are Sr $= +2.13 \pm 0.12$, Ti $= +4.27 \pm 0.35$ and O $= -2.13 \pm 0.27$, compared to the values expected for the perfect structure Sr $= +2.11$, Ti $= +4.14$ and O $= -2.08$. Additionally, at certain positions in the structure the valence of individual atoms varies by as much as ± 1 from the expected formal valences. (Note that the standard deviation for the strontium atoms is less than that for the other elements because the majority of the atom positions are on the edge of the structure. Outside the structure, atom columns are assumed to be in their bulk lattice sites.)

For the perfect unit cell structure, the occurrence of lattice sites where the valence deviates by ± 1 from the formal valence of the element is unlikely. However, we know that the heavy-element column positions in the structure are subject to an experimental error of ± 0.2 Å. Therefore, if we allow the column positions to move within the experimental error, we can check to determine whether a structure exists in which the formal valences of the elements agree with the expected values. Effectively we are performing a minimization of the bond-valence sum for all elements in the structure within the boundaries controlled by the experimental results. The aim of the minimization is to obtain the structure which contains the smallest deviation from the expected formal valence of the elements. It can be performed using an application program from the standard Microsoft Excel spreadsheet [57]. The simplicity of the bond-valence function allows the minimization program to run a structure of up to 200 atom column positions in a few hours on a standard Power Macintosh computer. Minimizing the structure in figure 4(*b*) gives the structure in figure 4(*c*), in which no individual atom position is more than 0.1 Å removed from the crystal lattice site and no valence is more than ± 0.1 from the expected values (Sr $= +2.13 \pm 0.04$, Ti $= +4.15 \pm 0.03$ and O $= -2.09 \pm 0.02$). The minimization does not produce the exact crystallographic lattice for $SrTiO_3$ without significantly more processing time and user control of movement parameters, but the removal of sites at which the valence deviates greatly from the expected value is routine and reproducible for all starting conditions within the 0.2 Å average error.

The bond-valence-sum technique is also useful for identifying errors in atomic column composition. For example, if in the structure in figure 4(*c*) one of the titanium columns were mistakenly identified as a strontium column, then the resulting minimization would produce the structure in figure 5(*a*). The average valences for the structure are Sr $= +2.27 \pm 0.19$, Ti $= +4.15 \pm 0.15$ and O $= -2.08 \pm 0.18$. By simple counting of the atomic columns present, the structure is charge neutral. However, if we look at the individual atomic columns, in the region of the mistaken column the valences can differ by as much as $+1$ from the expected values (shown by the shaded circle in figure 5(*a*)). This points directly to the offending atomic column, which has the greatest deviation from the expected valence, and suggests that an alternative starting structure should be used. The same behaviour is observed if one of the strontium columns is labelled as titanium (figure 5(*b*)). It can also be seen that the presence of the mistaken

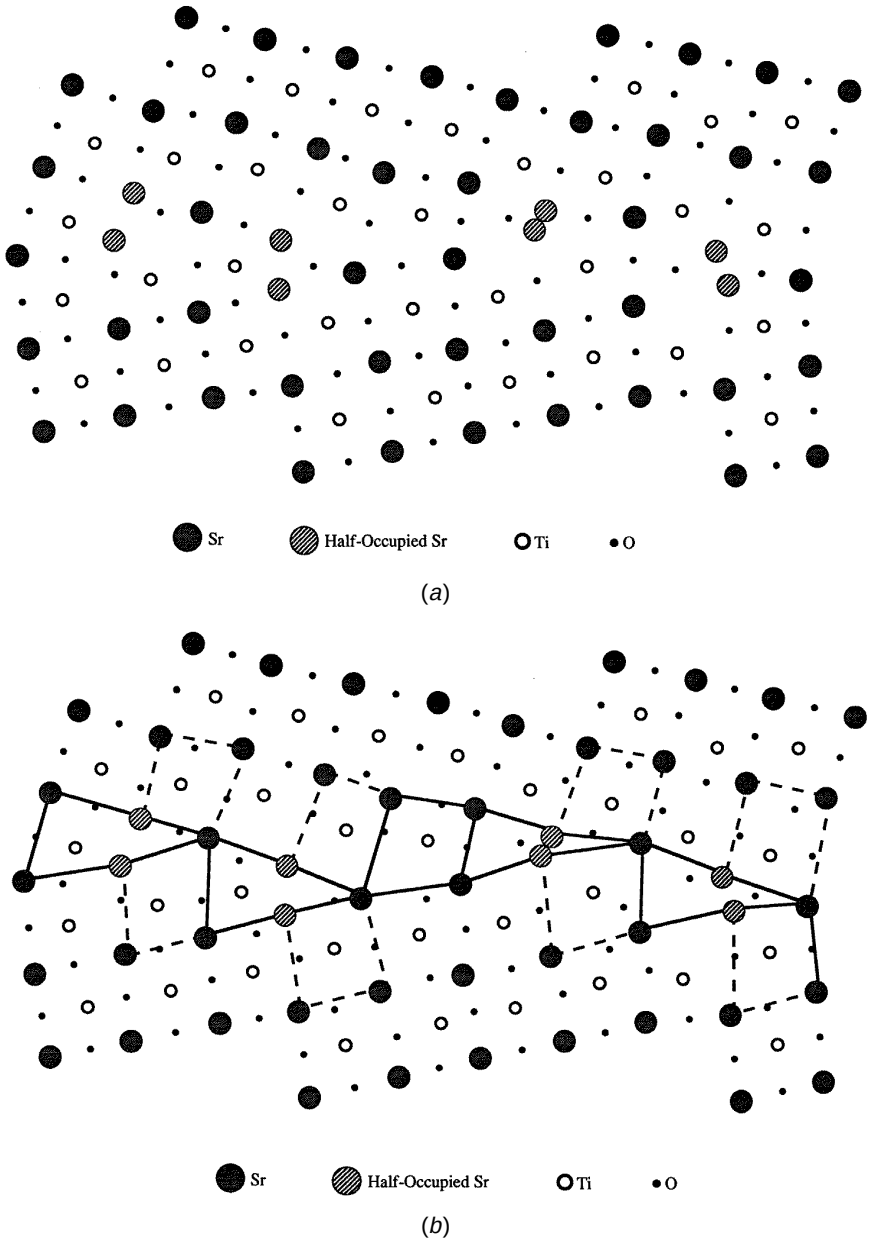

Figure 8. (*a*) A model structure for the 25° (920) grain boundary in which the oxygen columns are placed equidistantly between the metal columns. The shaded columns in (*a*) cannot be explained in terms of experimental factors such as tilting and, if they are assumed to be half occupied, the structure can be refined by bond-valence calculations to propose a model which is both charge neutral and stoichiometric (*b*). Comparison with the maximum entropy object function reveals that the movements of the metal columns required to produce a charge-neutral structure are less than the 0.2 Å accuracy of the object function.

columns in the structures destroys the fourfold symmetry of the final bond-valences-sum model. This feature is caused by the nature of the bond-valence minimization. The structures shown here and in the remainder of this paper are the result of a single minimization, namely a single minimization moving the atom with the biggest discrepancy and moving on to the next worst atom column position and so on. As has been stated previously, the accuracy of this result could be increased by more iterations and by starting from several different trial structures to obtain the lowest valence discrepancy. However, although these are standard techniques for detailed theoretical modelling of atomic structures at interfaces, their use is not warranted for our bond-valence-sum minimizations. It is not clear whether the accuracy of the bond-valence-sum calculations can permit the determination of a single model with high confidence. In our work, we use bond-valence minimizations only to test whether the experimentally determined structures obey crystal chemistry principles and not to derive a structure from first principles.

In figure 5 it is relatively straightforward to see that there is an error in the structure even without the

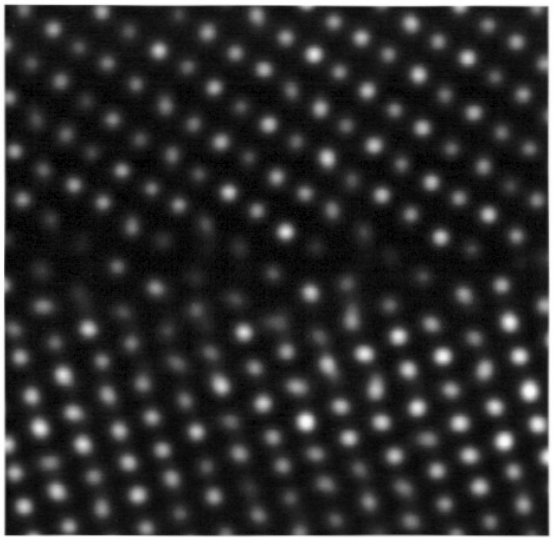

(*a*)

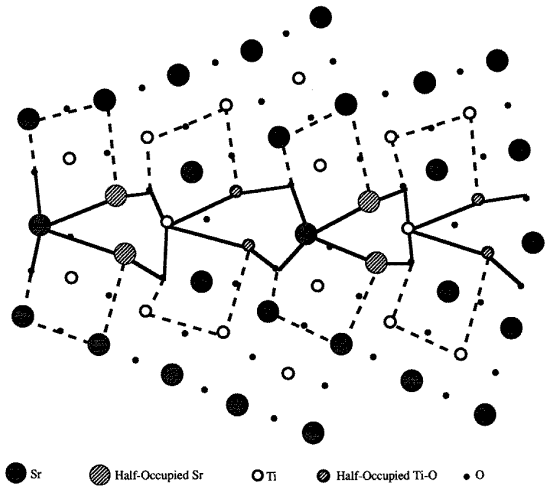

(*b*)

Figure 9. (*a*) The maximum entropy object function of a 36° (310) [001] tilt grain boundary in $SrTiO_3$. (*b*) The refinement of the structure by bond-valence calculations again leads to a model which is both charge neutral and stoichiometric. Comparison with the maximum entropy object function reveals that the movements of the metal columns required to produce a charge-neutral structure are less than the 0.2 Å accuracy of the object function.

bond-valence-sum minimizations, because the strontium (figure 5(*a*)) and titanium (figure 5(*b*)) spacings are too close. However, at interfaces where the composition contrast is masked by the second-order effects described earlier, this assists in the identification of the atomic columns in the interface plane. In particular, in cases in which atomic columns appear to be too close together and partial occupancy is assumed, this feature enables different compositions to be tested (see later sections).

4. Experimental characterization of [001] tilt grain boundaries in $SrTiO_2$

The study of grain boundary structures was performed with bicrystal samples, purchased in bulk form from Shinkosha Ltd, Tokyo, Japan. Specimens with the boundary parallel to the beam direction were thinned to electron transparency by mechanical dimpling and ion-beam milling. The ion milling procedure was performed at liquid nitrogen temperatures, at an angle of 15°, with an accelerating potential of 6 kV and 0.5 mA current until perforation, at which point the accelerating potential was reduced in steps to a minimum of 2 kV as the angle was increased to a maximum of 30°. This increase in angle accompanied by a decrease in accelerating potential was found to decrease the amount of ion-milling damage to the specimen significantly.

4.1. Symmetric grain boundaries

Figure 6 shows the maximum entropy object function for a 25° ($\Sigma = 85$) symmetric (920) boundary in a $SrTiO_3$ bicrystal [37]. Energy loss spectra taken from the bulk and boundary are shown in figure 7. Energy loss spectra were acquired in 4 Å steps across the boundary to give a profile of the changes in local coordination and formal valence with single-unit-cell resolution. The spectrum acquisition times were limited to < 5 s and acquired in the linescan mode of the microscope to reduce beam damage. In this mode the microscope probe is rapidly scanned in a line, the length of which is determined by the magnification of the microscope with the width being defined by the probe diameter. Because, for this study, the interest is in the changes in local coordination and formal valence perpendicular to the boundary, this acquisition mode allows the probe to be scanned in a line parallel to the boundary, thus reducing the electron dose at any particular atom site.

The titanium L edge shows no change in onset position, relative intensity of the L_2 and L_3 edges, or total L_2 plus L_3 edge intensity, which is indicative of there being no change in titanium formal valence or coordination [39–42]. The oxygen K edge shows similar behaviour, with the only difference between the bulk and the boundary being a change in the relative intensity of the π^* and σ^* peaks. This change can be interpreted in terms of a slight disorder of the linear Ti–O chains at the boundary [58]. The scan across the boundary indicates that the disorder of the linear Ti–O chains occurs over a width of two or three unit cells either side of the grain boundary [59]. These results indicate that the titanium in the boundary has the same coordination as has that in the bulk.

Using the atom column positions from the maximum entropy object function, the oxygen columns can be placed equidistant between the metal columns (figure 8(*a*)), thus preserving the Ti–O chains and the titanium coordination. The interesting feature in this structure is the occurrence of two strontium columns in close proximity (shaded) at regular intervals along the boundary. Because the strontium–strontium spacing in all materials is about 4 Å, the presence of these two columns cannot be explained in terms of experimental factors such as tilting. The probable

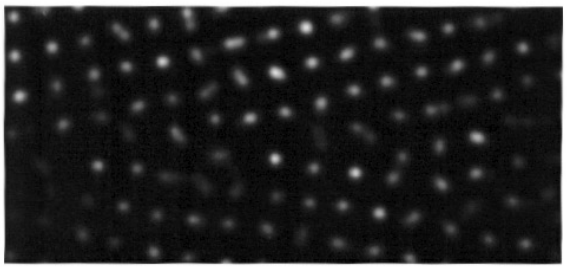

(*a*)

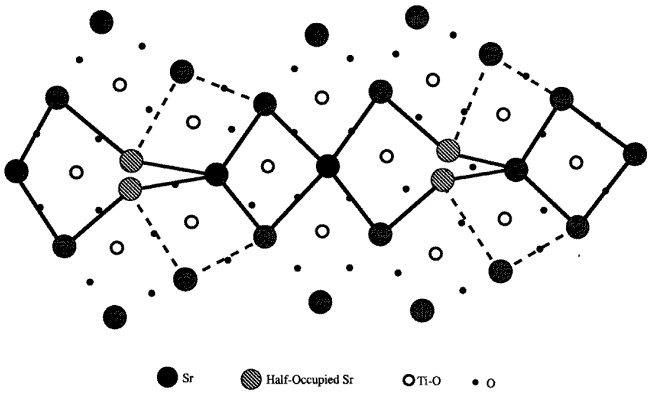

(*b*)

Figure 10. (*a*) The maximum entropy object function of a 67° (320) [001] tilt grain boundary in $SrTiO_3$. (*b*) The refinement of the structure by bond-valence calculations leads to a model which is both charge neutral and stoichiometric. Comparison with the maximum entropy object function reveals that the movements of the metal columns required to produce a charge-neutral structure are less than the 0.2 Å accuracy of the object function.

explanation of these features is that each column is not fully occupied. The simplest partial occupancy is with each column being alternately occupied through the thickness of the sample, because this preserves the Sr–Sr spacing at around 4 Å. An equivalent interpretation is to consider the two columns as a single column that alternates between the two crystals either side of the boundary in unit cell steps through the thickness of the sample.

Incorporating this half column principle and using the positions of the other columns from the maximum entropy object function, the bond-valence-sum minimization was performed to refine the structure (figure 8(*b*)). Consistent with the spectroscopic data indicating that the majority of the disorder takes place within two or three unit cells of the grain boundary, atom positions outside this range were used as fixed references for the bond-valence minimization. The average valence for each of the constituent atoms was determined to be Sr $= +2.09 \pm 0.11$, Ti $= +4.10 \pm 0.09$ and O $= -2.07 \pm 0.16$. At no position did the valence differ by more than 0.4 from the average value. Additionally, at no site in the structure was a metal atom column moved by more than the 0.2 Å positional error expected from the maximum entropy analysis. Also observed in the structure are positions in the grain boundary plane where the expected Ti–O column is missing. Again this feature cannot be attributed to experimental artefacts and is consistent with the reduction in distance to the surrounding columns to maintain charge neutrality. (Note that a 50% occurrence of missing columns results in the grain boundary plane maintaining the bulk stoichiometry.)

This same analysis has been performed for the symmetric 36° ($\Sigma = 5$) (310) (figure 9(*a*)) and 67° ($\Sigma = 13$) (320) boundaries (figure 10(*a*)). In the 36° boundary there appear to be sites where both strontium and titanium columns are separated by significantly smaller distances than the bulk values, whereas for the 67° boundary only strontium columns in the boundary plane appear too close. Using a similar half column occupancy argument as for the 25° boundary, bond-valence-sum calculations can be used to refine the structure and propose a model in which the boundary is again stoichiometric and charge neutral (figures 9(*b*) and 10(*b*)). The average valences were determined to be Sr $= +2.12 \pm 0.10$, Ti $= +4.06 \pm 0.10$ and O $= -2.08 \pm 0.19$ for the 36° boundary and Sr $= +2.17 \pm 0.18$, Ti $= +4.03 \pm 0.09$ and O $= -2.05 \pm 0.19$ for the 67° boundary (again at no position did the valence differ by more than 0.4 from the average or were the columns shifted by more than 0.2 Å) [57].

4.2. Asymmetric grain boundaries

Figure 11(*a*) shows the maximum entropy object function of a 45° asymmetric grain boundary in $SrTiO_3$ which is faceted along the (100) and (110) planes. The energy loss spectra showed similar results to the symmetric boundaries with the only observable change being in the ratio of π^* to σ^* peaks in the oxygen K edge [61]. Performing

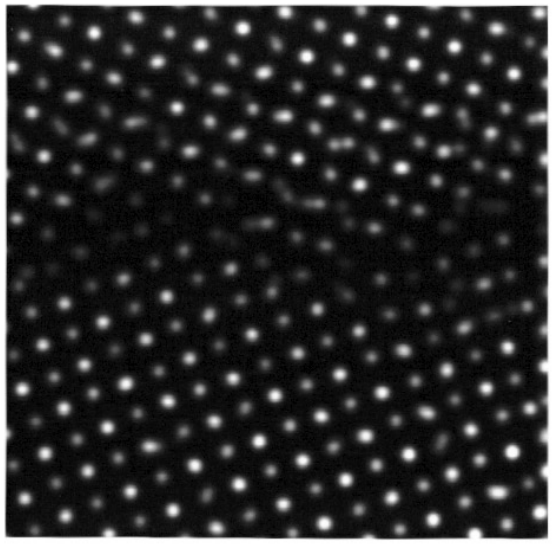

(*a*)

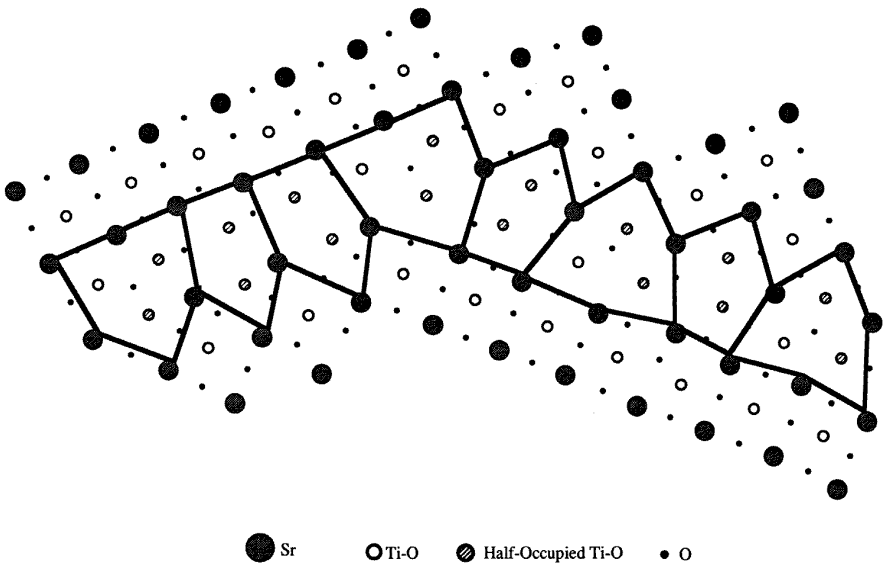

(*b*)

Figure 11. (*a*) The maximum entropy object function of an asymmetric 45° [001] tilt boundary in $SrTiO_3$. (*b*) The bond-valence-sum-minimized structure for the boundary, again incorporating half columns (shown hatched) (Sr = +2.14 ± 0.06, Ti = +4.14 ± 0.05 and O = −2.08 ± 0.10).

bond-valence minimization in the same manner as for the symmetric boundaries yields the structure shown in figure 11(*b*). The average valences of the constituent atoms were Sr = +2.14 ± 0.06, Ti = +4.14 ± 0.05 and O = −2.08 ± 0.10, with again no individual valency variations of greater than 0.4 and no shifts of more than 0.2 Å. It can be seen in figure 11(*b*) that there exist positions where Ti–O columns are too close together. In these positions the columns were again considered to be half occupied. Since the boundary was determined to be symmetric on the macroscopic scale, this microfaceting indicates that it is energetically more favourable for these materials to form faceted boundaries than symmetric grain boundaries. (This observation is consistent with those made by Merkle and Wolf [62].) By constructing a series of (100) and (110) planes across the grain boundary, a contraction of 0.56 ± 0.16 Å normal to the boundary plane was measured according to the method described by Merkle [63]. The grain boundary contraction is contained within the boundary region and was measured across all 12 (100)/(110) facets studied in this 45° asymmetric boundary [61].

Figure 12(*a*) shows the maximum entropy object function of an asymmetric (100)/(940) facet region in a 25° $SrTiO_3$ bicrystal, where the majority of the boundary is symmetric with a (920) common boundary plane. Using the cation coordinates obtained from the maximum entropy analysis the (100) planes on one side of the grain boundary and a series of corresponding (940) planes for each unit cell on the other side of the grain boundary were calculated. A 0.5 ± 0.2 Å dilation normal to the boundary plane was

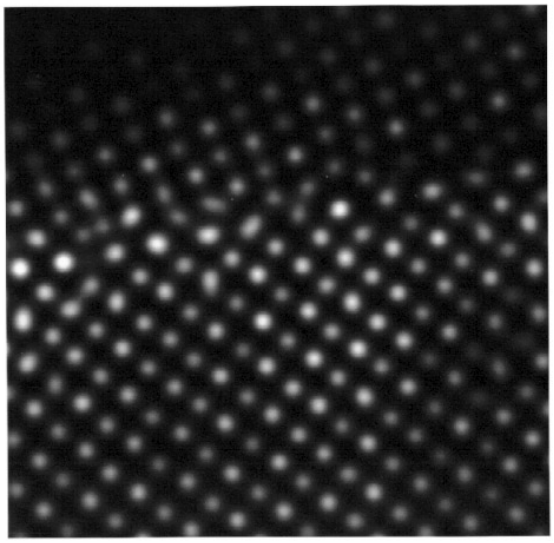

(*a*)

(*b*)

Figure 12. (*a*) The maximum entropy object function of an asymmetric facet in a 25° [001] tilt boundary in $SrTiO_3$. (*b*) The bond-valence-sum-minimized structure (Sr = +2.18 ± 0.19, Ti = +4.17 ± 0.17 and O = −2.13 ± 0).

measured in this asymmetric facet [61]. This is consistent with a dilation of 0.6 ± 0.2 Å [35] in the symmetric portion of the boundary and is to be expected since any dilation of the short asymmetric facet is necessarily constrained by the dilation of the symmetric regions predominant in this boundary. Just as before, the cation coordinates obtained from the maximum entropy analysis and the octahedral Ti–O coordination from EELS were combined to construct a structure model for the 25° asymmetric grain boundary in $SrTiO_3$. Figure 12(*b*) shows the grain boundary structural model for this 25° boundary after bond-valence-sum calculations. (The average valences are Sr = +2.18±0.19, Ti = +4.17±0.17 and O = −2.13±0.20 with the same restrictions on individual valences and positional shifts as for the other boundaries.)

5. Structural units and continuity of [001] tilt boundary structure in $SrTiO_3$

5.1. Symmetric grain boundaries

From the experimental images of the 25°, 36° and 67° symmetric boundaries it can be seen that they are composed of distinct repeating 'structural units' (figure 13). These units can be combined to produce structures for all [001] symmetrical tilt grain boundaries in the range 0–90°, as is illustrated in table 1 for boundaries with $\Sigma < 41$. The ends of the series, the A and A* units, correspond to a (100) and a (110) boundary plane respectively. The B, B', C and D units correspond to the favoured boundaries in the terminology of Sutton and Vitek [22], in which the boundary is composed entirely of one type of structural unit, each of which represents the termination of one or more perfect lattice dislocations in the Read–Shockley model

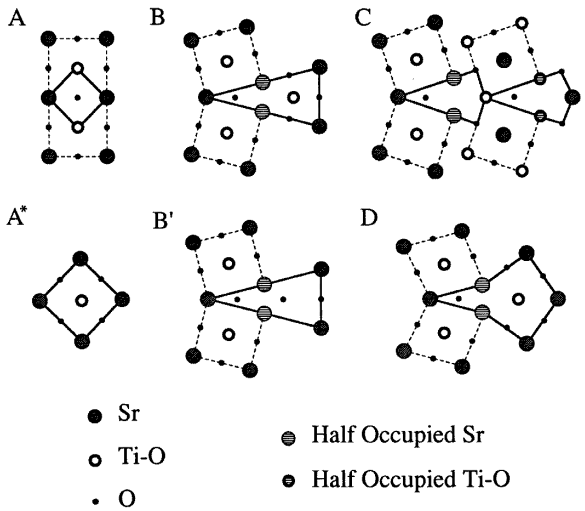

Figure 13. Six 'structural units' can be identified from the experimental boundaries. The A unit corresponds to a (100) boundary plane, the A* unit to a (110) boundary plane, the B and B′ together to a (410) boundary plane, the C unit to a (310) boundary plane and the D unit to a (210) boundary plane.

Table 1. The six structural units in figure 8 can be combined to compose all the [001] tilt boundaries with $\Sigma < 41$ consistent with continuity of grain boundary structure models.

Boundary plane	θ	Σ	Structure
$(10\bar{0})_1/(100)_2$	0	1	A
$(9\bar{1}0)_1/(910)_2$	12.68	41	AABAAB′A
$(7\bar{1}0)_1/(710)_2$	16.26	25	ABAB′A
$(6\bar{1}0)_1/(610)_2$	18.92	37	ABAB′
$(5\bar{1}0)_1/(510)_2$	22.62	13	BAB′
$(4\bar{1}0)_1/(410)_2$	28.07	17	BB′
$(3\bar{1}0)_1/(310)_2$	36.87	5	C
$(5\bar{2}0)_1/(520)_2$	43.60	29	CD
$(7\bar{3}0)_1/(730)_2$	46.40	29	DCD
$(2\bar{1}0)_1/(210)_2$	53.13	5	D
$(5\bar{3}0)_1/(530)_2$	61.93	17	DA*D
$(3\bar{2}0)_1/(320)_2$	67.38	13	DA*
$(7\bar{5}0)_1/(750)_2$	71.08	37	A*DA*DA*
$(4\bar{3}0)_1/(430)_2$	73.74	25	A*DA*
$(5\bar{4}0)_1/(540)_2$	77.32	41	A*A*DA*
$(1\bar{1}0)_1/(110)_2$	90	1	A*

[64]. Such a boundary has a perfectly periodic dislocation spacing and thus no long-range strain fields.

For the C unit this corresponds to the (310) $\Sigma = 5$ boundary plane and for the D unit this corresponds to the (210) $\Sigma = 5$ boundary plane. Both of these units terminate two lattice dislocations and are thus symmetrical about the boundary plane. The B and B′ units terminate a primitive lattice dislocation and therefore introduce asymmetry into the boundary structure. The difference between the B and B′ units is the presence or absence of one TiO column. This makes the B repeat unit strontium-deficient and the B′ unit strontium-rich. However, as is observed in the image of the {920} boundary, an equal mixture of both of these units results in stoichiometric boundary plane. The smallest repeat structure that contains both of these units is the $\{410\}\Sigma = 17$ boundary plane and this again corresponds to a favoured boundary in which there are no other units present. This structure has to be considered a combination of B and B′ units rather than a single $B^* = BB'$ unit, because, for a single repeat unit, continuity of grain boundary structure would dictate that the B and B′ units be adjacent at all boundary misorientations below the 28° of the {410} boundary. However, as can be seen in table 1, for angles below 28° the B and B′ units can be separated as uniformly as possible by A units. This behaviour is consistent with a reduction in the grain boundary energy by equal distribution of the grain boundary dislocation cores. The B and B′ structural units should therefore be regarded as alternative possible units.

Over the entire range of boundary misorientations the rules of continuity of grain boundary structure outlined by Sutton and Vitek [22, 23] are followed; that is, for boundary misorientations between the favoured boundaries the structure is composed of a mixture of the structural units of these boundaries, in which each minority forms the core of a secondary dislocation required to account for the difference in angle from the favoured misorientation [60]. To illustrate this behaviour figure 14 shows a $\Sigma = 73$ {830}, 41.11° boundary with the sequence CDC. Each D unit forms the extended core of a $\boldsymbol{b} = (2/10)\langle 310\rangle$ secondary grain boundary dislocation having again twice the primitive Burgers vector. Such behaviour is very similar to that found for FCC metals. A new feature, however, is the appearance of significant numbers of half columns in adjacent units. In the C units of figure 14 half columns lie in the {310} plane either either side of the boundary plane and must therefore be considered as half planes. Therefore two {310} planes, one from each crystal, become half planes at a minority D unit and combine at the next D unit to form a full {310} boundary plane which then terminates at the following D unit.

Grain boundaries composed of the B and B′ units contain an additional complexity. Since they represent the cores of primitive lattice dislocations the boundary is not microscopically symmetric and is better interpreted as a series of microfacets (figure 15). The actual faceted boundary plane is shown as a bold line and lies along a {100} plane of one of the crystals. Note that it is asymmetrically located with respect to the macroscopic {410} boundary plane that contains the coincident lattice sites (crossed symbols). This implies that all boundaries below the $\Sigma = 5$ {310}, 36.87° boundary are microscopically asymmetric. Calculations by King and Smith [65] suggested that the energy cost of microfaceting might be considerable, even for small misorientations inducing pairs of dislocations to associate and form a straight symmetric boundary plane. However, using the energy of a hollow core dislocation [66], which in view of the half columns in our structural units may be most appropriate, coalescence is predicted for angles above 29° [60]. This is in good agreement with observation, although clearly the angle is very sensitive to the core description chosen and better estimates could be obtained through

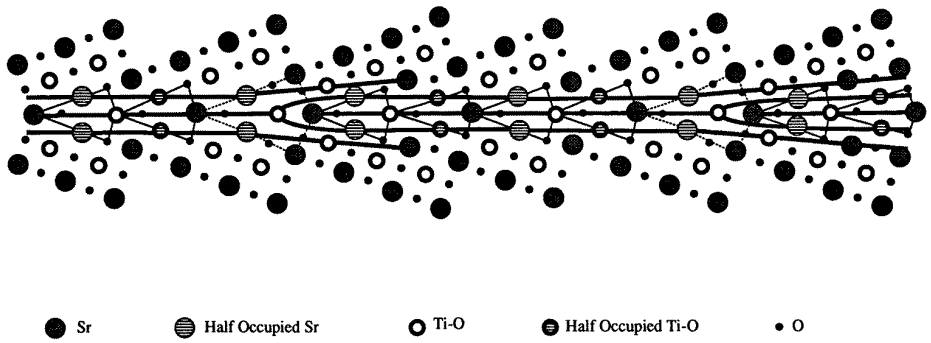

Figure 14. In the $\Sigma = 73$ {830}, 41.11° boundary, each D unit forms the extended core of a $\boldsymbol{b} = \langle 2/10 \rangle \langle 310 \rangle$ secondary grain boundary dislocation.

atomistic simulations. However, it is clear that primitive dislocations are not unexpected at small angles. Similar considerations can also be used to show that the lowest energy faceted boundary occurs when all the displaced dislocations lie to one side of the macroscopic boundary plane [60]. Consider reflecting every alternate B unit, so that the macroscopic boundary plane passes through centre of the facets. The component of the Burgers vector perpendicular to the boundary plane now has a similar strain energy to an array of dislocations with Burgers vector $2\boldsymbol{b}$ and spacing $2R$, and therefore has twice the boundary energy.

5.2. Asymmetric grain boundaries

Similarly to the symmetric boundaries, three distinct grain boundary structural units can be identified in the experimental images of the 25° and 45° asymmetric [001] tilt boundaries (figure 16). The B and C units represent the termination of perfect lattice dislocations at the grain boundary while the A unit is a (100) 'spacer unit'. This number of structural units is consistent with the need for two types of dislocation cores to describe an asymmetric grain boundary. The dislocations represented by the B and C structural units are illustrated in figure 17 which shows a segment of the predicted grain boundary structure for the 18.4° (100)/(310) asymmetric grain boundary. From figure 17 we can see that the B unit consists of a $\langle 100 \rangle$ dislocation and that the larger C unit can be considered as the combination of a $\langle 100 \rangle$ and a $\langle 010 \rangle$ dislocation. Therefore we consider the C unit to contain a B unit in this description. The required spacings of the $\langle 100 \rangle$ and $\langle 010 \rangle$ dislocation cores are obtained from the Read–Shockley model [64] as $D_B = 1/\sin\theta$ and $D_C = 1(1 - \cos\theta)$ respectively. These spacings are given in table 2.

Again, these grain boundary structural units can be used to predict the structure for other misorientations by applying the principle of continuity of boundary [61]. Consider first application of the technique to the 45° boundary, which need only comprise B and C units. The structure of the 45° boundary can be predicted simply by applying the strip method described by Sutton [23] to determine the correct sequence of B and C units, as illustrated in figure 18. A

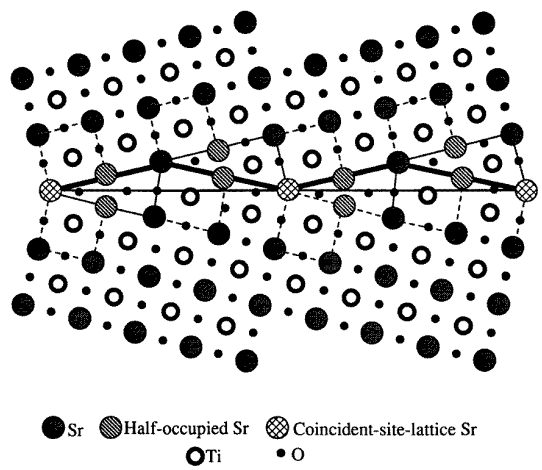

Figure 15. At misorientations below the 28.07° of the (410) $\Sigma = 17$ boundary, the boundary plane can be interpreted as a series of microfacets.

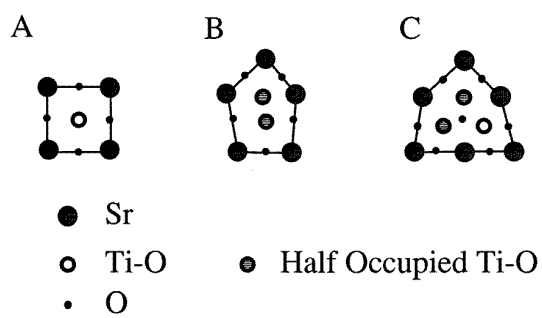

Figure 16. The three distinct grain boundary structural units identified experimentally in the asymmetric [001] tilt boundaries of $SrTiO_3$. The A unit corresponds to a (100) boundary plane, the B unit to a (110) boundary plane and the C unit to a (110) boundary plane.

line is drawn to pass through the origin (0,0) and intercept at $(1, m)$, where m is the ratio of C:B units calculated from the dislocation spacings D_B and D_C given in table 2 (bearing in mind that the C unit contains a B dislocation core). For the 45° boundary the ratio of C:B units is

Table 2. The three distinct grain boundary structural units of figure 8 can be combined to construct other [001] tilt boundaries in $SrTiO_3$ by applying the principle of continuity of grain boundary structure in two stages, one for each type of dislocation.

Boundary plane	θ	D_B	D_C	m	Basic sequence
$(100)_1/(100)_2$	0				A
$(100)_1/(510)_2$	11.4	5.10a	51.50a	0.110	AAAAG
$(100)_1/(410)_2$	14.0	4.12a	33.49a	0.140	AAAG
$(100)_1/(310)_2$	18.4	3.16a	19.49a	0.194	AAG
$(100)_1/(210)_2$	26.56	2.24a	9.47a	0.309	AG
$(100)_1/(320)_2$	33.7	1.0a	5.95a	1.868	AGG
$(100)_1/(110)_2$	45.0	1.41a	3.41a	0.707	G

Table 2. (Continued)

Boundary plane	Unit 1	Unit 2	Grain boundary structure
$(100)_1/(100)_2$			
$(100)_1/(510)_2$	$(AAAAB)_9(AAAAC)$	$(AAAAB)_{10}(AAAAC)$	$(1)_{10}2(1)_9 2(1)_9 2(1)_9 2\ldots$
$(100)_1/(410)_2$	$(AAAB)_7(AAAC)$	$(AAAB)_8(AAAC)$	$(1)_8 2(1)_7 2(1)_7 2(1)_7 2\ldots$
$(100)_1/(310)_2$	$(AAB)_5(AAC)$	$(AAB)_6(AAC)$	$(1)_6 2(1)_5 2(1)_5 2(1)_5 2(1)_5 2(1)_6 2\ldots$
$(100)_1/(210)_2$	ABABABAC	ABABABABAC	$(1)_4 2(1)_3 2(1)_3 2(1)_4 2\ldots$
$(100)_1/(320)_2$	ABC	ABBABC	121221212212122122...
$(100)_1/(110)_2$	BC	BBC	BBCBCBBCBCBBCBCBC...

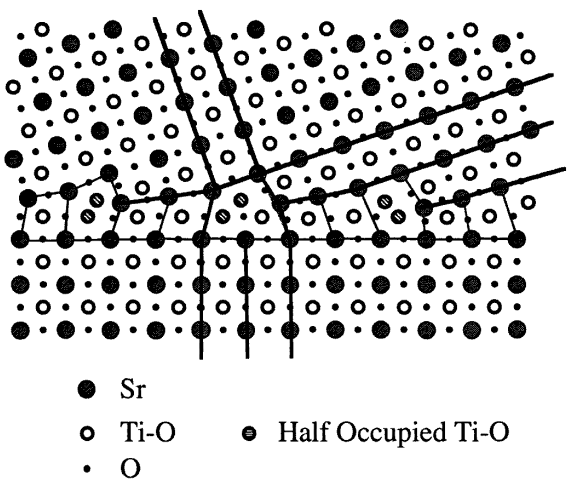

Figure 17. A schematic diagram of the grain boundary dislocation cores represented by the B and C grain boundary structural units in an asymmetric 18.4° (100)/(310) grain boundary.

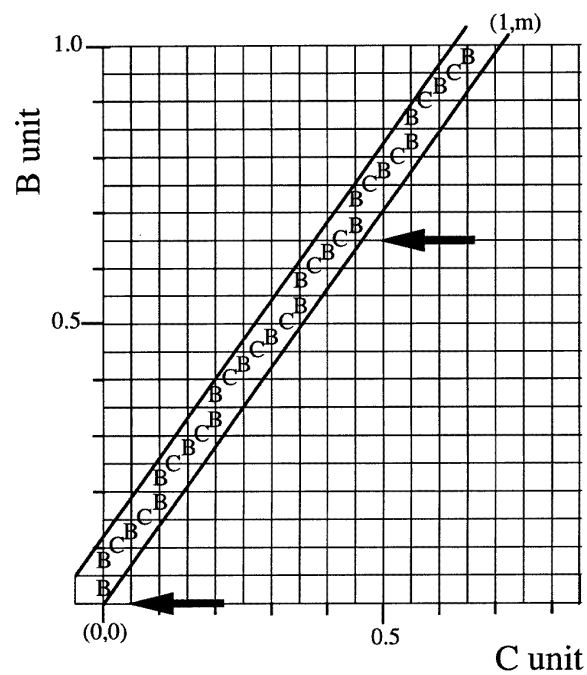

Figure 18. A schematic illustration of the strip method described by Sutton [23] for the 45° boundary. The sequence of B and C units is given by following the grid squares between the parallel lines such that a step along the B axis corresponds to a B unit in the boundary sequence. For the portion of the 45° (100)/(110) boundary shown here the grain boundary structure is given as BBCBCBBCBCBBCBCBCBBC... and so on.

$m = 0.707$. A second line is drawn parallel to the first but separated by the length of a diagonal of the unit squares. The sequence of boundary units is then given by following the grid squares between the parallel lines such that a step along the B axis corresponds to a B unit in the boundary sequence. The segment of the 45° (100)/(110) boundary represented in figure 18 shows a grain boundary structure of BBCBCBBCBCBBCBCBCBBC... and so on. (Since the boundary is only quasi-periodic there is no exact repeat structure.) The exact portion of the sequence of B and C units represented in figure 18 is dependent on the position of the origin; the sequence of the facets in figure 11(*b*) corresponds only to a small section of this boundary.

For misorientation angles below 45°, there is an additional degree of freedom, namely that associated with the A unit. This means that the asymmetric grain boundaries will not show continuity of boundary structure over the whole misorientation range since the spacings of the two dislocation cores have different dependences on

misorientation. Nevertheless, it is still possible to predict the grain boundary structure by applying the principle of continuity of boundary structure in two stages [61]. The first stage is to define a generic (110) unit. Since the B and C units have the same boundary translation vector, we can apply the principle of continuity to determine the sequence of A and G units. Just as with the symmetric grain boundaries, the A and G units represent favoured boundaries and any boundary misorientation between these favoured boundaries is constructed of a suitable combination of A and G units, as shown in table 2. This combination we will refer to as the basic boundary sequence. The second stage is to convert the generic unit into B and C units in the correct ratio for the boundary misorientation. To do this we note that the correct average spacing of the B dislocations, D_B, is specified by the basic sequence of the boundary. This is because each G unit contains a B dislocation, whether we convert it to a B unit or a C unit. Therefore, we need only consider how to achieve the correct average spacing of C units along the boundary. The C units have a larger spacing along the boundary than do the B units and we define this average spacing as a multiple, q, of the basic sequence length, where $q = D_C$/sequence length. For the quasi-periodic boundaries q has a non-integer value. This non-integer value of q can be accommodated by the combination of two new boundary units, unit 1 and unit 2, comprising d_1 and d_2 basic sequences, respectively, where d_1 and d_2 are integers closest to q, such that $d_1 < q < d_2$. We place one C unit in each new unit and combine them using the strip method described previously to determine the correct sequence of units 1 and 2.

It is perhaps easiest to illustrate this procedure with a specific example. From table 2, the basic boundary sequence for a 18.4° (100)/(310) boundary is AAG and $q = 6.16$, giving $d_1 = 6$ and $d_2 = 7$. We therefore define unit 1, which has a length of d_1 basic sequences, to be $(AAB)_5(AAC)$ and unit 2, which has a length of d_2 basic sequences, to be $(AAB)_6(AAC)$. The correct C spacing is achieved by applying the strip method to units 1 and 2 in the ratio m, where m is now given by

$$m = (q - d_1)/(d_2 - q).$$

The sequence of units 1 and 2, obtained from the strip method is 11111211111121111121... and so on. By substituting the units $(AAB)_5(AAC)$ and $(AAB)_6(AAC)$ and for units 1 and 2, respectively, the grain boundary structure can be predicted.

Predicted structures for other misorientations are summarized in table 2. In the case of the 33.7° (100)/(320) boundary, there is the possibility of structural multiplicity due to the more complicated nature of the basic boundary sequence, AGG. There are now two ways to define unit 1, either as ABC or as ACB which we will denote 1′. Similarly, unit 2 can be defined either as ABBABC or as ABBACB which we will denote 2′. The predicted boundary structure is 121221212212122122... and so on. If we accept that 1 and 1′ and 2 and 2′ are geometrically equivalent then we have four possibilities for the sequence 2 1, namely

2 1 ABBABCABC

2′1 ABBACBABC

2′1′ABBACBACB

2 1′ABBABCACB

We may predict that 2′ precedes 1 since this configuration evens out the spacing of the C units and thus minimizes the grain boundary energy. However, in the sequence 2 2 1 it is possible to have either 2 2′ 1 or 2′ 2′ 1 since they both have the same average spacing of the C units. It may be that in these cases involving structural multiplicity a more detailed prediction could be achieved by extending the strip method itself to three dimensions (corresponding to the three structural units A, B and C). However, it is clear that, for the simpler boundaries of table 2, this two-stage method does yield a single specific prediction for the grain boundary structure. Modification of the principle of continuity of grain boundary structure, for a system containing three grain boundary structural units, therefore enables the prediction of grain boundary structures for other misorientations in asymmetric [001] tilt boundaries of $SrTiO_3$. However, we emphasize that the final boundary structures do not explicitly show continuity of boundary structure since the spacings of the B and C dislocations have a different misorientation-dependence.

6. Discussion

The common feature in all of the experimental and modelled grain boundaries in this paper is the presence of half occupied atomic columns in the boundary plane. This feature of the grain boundaries is inferred directly from the experimental results. Transverse incoherence in the Z-contrast image permits the unambiguous identification of two atomic columns separated by distances in the range 1–2 Å. Incorporating the image with the energy loss spectra into bond-valence-sum minimization routines permits the composition of the columns, in terms of atomic species, to be identified. In all cases the columns in close proximity to each other were determined to contain like ions. Thus we have the classic like-ion repulsion problem for grain boundaries in ionic materials. It has long been appreciated that the solution to this problem is the incorporation of vacancies in the grain boundary structure [67, 68], a feature which has been indicated in previous high-resolution TEM studies of NiO [1] and NiAl [69]. Here we have assumed the simplest form of partial occupancy, namely 50%. Because the Z-contrast image does not permit the exact occupancy of the columns to be determined, this value for the occupancy represents the least possible disorder in the structure. This does not exclude the possibility that the occupancy is 60–40 and so on, but it must be noted that the occupancy is unlikely to be too one-sided because this would reduce the channelling effect in the image and cause on the columns to fade into the background.

In the models developed in this paper the two closest columns in each of the structural units were taken to be half occupied and included as such in the bond-valence-sum minimization. In reality, however, as we proceed through the thickness of the specimen, there will be places in which

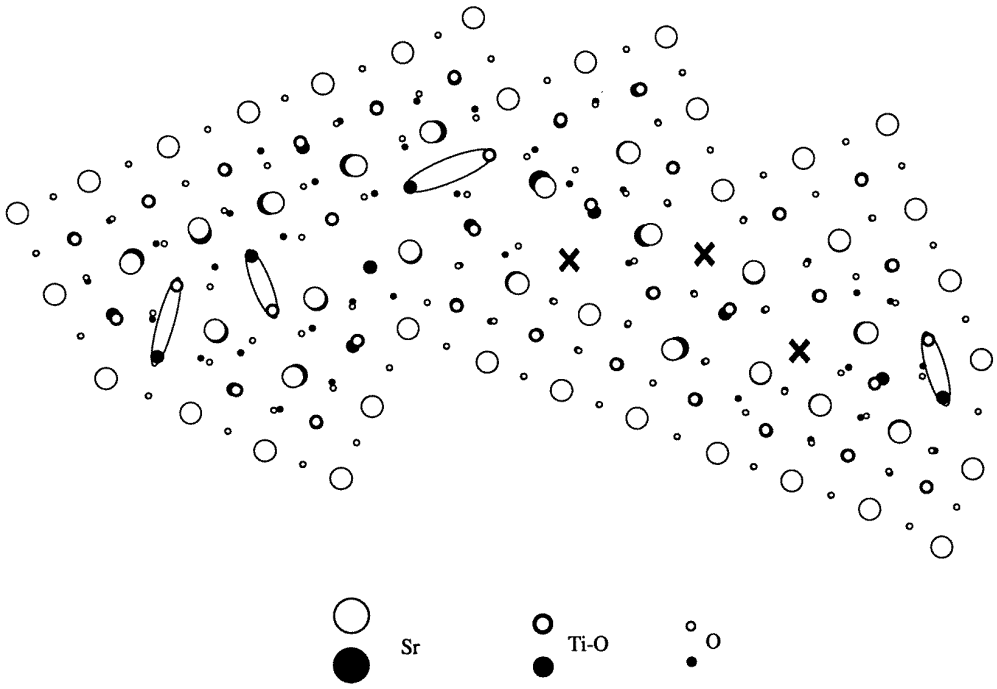

Figure 19. The superposition of two possible structures for the 45° asymmetric [001] tilt boundary shown in figure 11. Notice the majority of the movement comes from the oxygen columns which are not observed in the Z-contrast image. Additionally, the movement of the metal atoms decreases away from the centre of the structural units, in good agreement with the two or three unit cell width observed in the EELS profile.

one of the half column sites will be occupied and the other unoccupied. Additionally, for the large asymmetric units that are illustrated for the 45° boundary, there exists the possibility that the three Ti–O columns in the structure are a third occupied or that the half-occupancy shifts randomly between two of the three columns. In all of these cases there exists the possibility that the structure is different from that determined in the bond-valence minimizations. If we assume that, for this occupancy, the vacant sites will be distributed evenly, that is, no two vacant sites next to each other, then there are 11 possible starting structures for the 45° asymmetric boundary shown in figure 11. Each of these structures can be bond-valence-minimized separately. Shown in figure 19 are two representative structures superimposed to illustrate the relative change in atomic column positions for each structure. In cases in which the half occupied columns are the same for each model the vacant sites are marked with crosses. At positions where the half occupied columns differ, the two positions are linked for clarity. As can be seen, there is very little movement (< 0.1 Å) for the majority metal atom sites in each of the structures. Changes in metal atom occupancy are accommodated by variations in the positioning of the oxygen columns which are not observed in the Z-contrast image. The implication of this result is that by combining the Z-contrast image with EELS in the bond-valence-sum calculations we are not registering sensitively the presence of individual vacancies. The atomic column locations derived from the bond-valence-sum minimizations in this paper must therefore be viewed as showing the average position of the atoms through the thickness of the specimen. As is probably to be expected, the columns closest to the centre of the structural units exhibit more variation in position through the thickness of the material, because they are directly affected by the half columns. It is interesting to note that the length scale over which these distortions are reduced corresponds well with the two or three unit cells width of the boundary observed in the EELS profile [59].

This result indicates that the structural models produced by this technique are relatively insensitive to changes in column occupancy. To examine the effect of reduced occupancy on the bond-valence-minimized structure further, individual lattice vacancies can be introduced into the 4×4 unit cell structure studied previously. The minimized structures containing individual strontium (figure 20(a)), titanium (figure 20(b)) and oxygen (figure 20(c)) vacancies are compared with the perfect unit cell structure. In all three cases similar statistical results to those for the perfect crystal are produced (no lattice site$>$ ± 0.1 Å displaced and standard deviation about 0.05 for the valences). Again the majority of the differences among the models are directly related to the oxygen columns, with the metal atom positions being changed very little for all three structures. The titanium vacancy in figure 20(b) appears to have the greatest influence on the surrounding atomic column positions and this is probably due to titanium having the largest valency in the structure; that is, the surrounding atoms have to distort more to accommodate the larger change in valence. However, considering that an individual lattice vacancy in this example corresponds to a defect density of 10^{21} cm^{-3} indicates that the Z-contrast

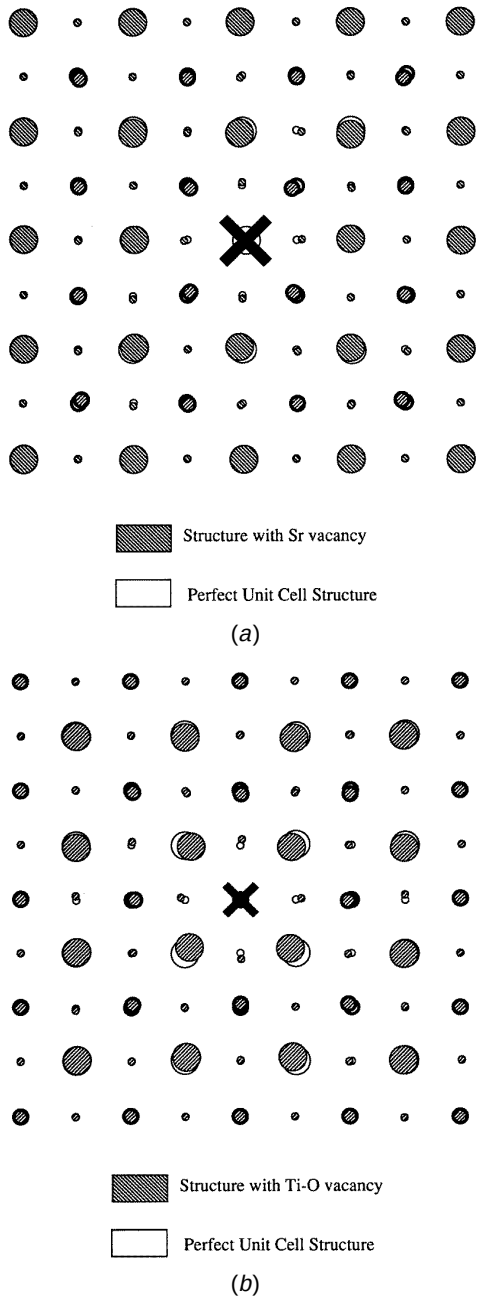

Figure 20. Bond-valence-minimized 4 × 4 unit cell blocks containing (*a*) a strontium vacancy, (*b*) a titanium vacancy and (*c*) an oxygen vacancy.

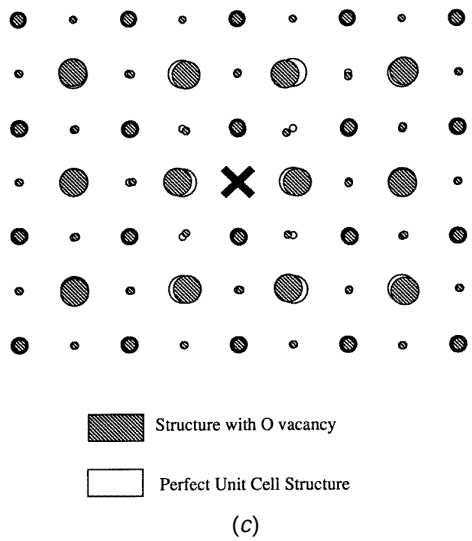

Figure 20. (Continued.)

technique is not able to identify individual lattice vacancy positions even at very high densities.

Observing lattice vacancies is therefore not possible using this combination of microscopical techniques. Even in setting up the experiment in such a way as to optimize the energy loss signal for compositional analysis, the statistics of the process mean that the result would only be accurate to within about 5–10%. The same is true for x-ray microanalysis and in both cases this is well above the requirement to observe vacancies with the required sensitivity. It may be possible to position the probe over a defined crystallographic location and observe changes in the energy loss fine structure [38], but this would require significantly improved statistics from the experimental spectrum. However, the density of lattice vacancies can be calculated from other techniques such as bulk transport measurements [70–73]. The insensitivity of the models produced by Z-contrast/EELS to lattice vacancies means that they are ideal starting points for theoretical calculations employing more sophisticated techniques for structure determination [74]. Including vacancy densities from bulk techniques with the Z-contrast/EELS method greatly reduces the amount of processing time by reducing the number of trial structures needed and eliminating false minima. The structural models produced also help in the interpretation of results from other microscopical techniques, such as electron holography, in which boundary effects are consistent with a reduced density over the two or three unit cell width observed here [74].

The half columns present in the dislocation cores of these models have important implications both for the mechanical and for the electrical properties of these materials. Movement of such a dislocation will necessarily involve lattice diffusion whether the dislocation moves in the conventional climb or rather in a glide direction, implying perhaps a high activation energy for grain boundary migration. It is somewhat misleading to regard the half columns as comprising lattice vacancies, since there is insufficient volume in which to place a matrix cation. However, these sites may be occupied by an amphoteric species, or, if we regard the structure as a single zig–zag column, then each cation clearly has an excess volume associated with it and could act as a preferential site for segregation of a cation of larger ionic radius by substitution. Additionally, the observation of two B-type units, with and without TiO columns, implies that these sites could also accommodate impurities of small ionic radius.

The present study has dealt only with undoped clean grain boundaries in $SrTiO_3$. However, it is well known that the electrical properties of this and other electroceramic materials can be controlled by the incorporation of dopants

which have a tendency to segregate at the grain boundaries [70–79]. Although the techniques described in this paper are not capable of observing individual vacancies, they are capable of observing the presence of dopant atoms of the order of one or two atoms per atomic column. This is simply due to the nature of the techniques. To quantify vacancies on a large signal requires a high degree of accuracy, whereas to observe the distinctive shape of a 'new' signal is much easier. When coupling this with the ability to pick out individual atomic columns, it means that likely segregant sites can be identified in the image initially, thereby reducing the area of study and increasing the current density on the dopant atoms.

7. Conclusions

Presented in this paper is a direct experimental technique for determining the atomic structure, composition and bonding at internal interfaces using combined Z-contrast imaging and EELS at atomic resolution. The experimental conditions both for the image and for the spectrum can be tailored to give incoherent signals, allowing the intuitive interpretation of the experimental results with the spatial resolution of the electron probe (2.2 Å). The analytical signal can therefore be related directly to the atomic structure observed in the image and, through bond-valence-sum analysis, model structures for interfaces can be developed which obey crystal chemistry principles. Such models should not be viewed as definitive structure determinations, but they are nonetheless derived from direct experimental evidence. As such the models are different from conventional TEM images that require simulations to interpret interface structures on the atomic scale. TEM images can be compared to extensive theoretical calculations; these models, in contrast, start from preconceived structures which are limited by the ability of the operator to pick the correct initial conditions. For non-periodic or large repeat structures there is the added complication that computational requirements are beyond that which is currently available. Additionally, a match with the image only shows that the particular structure simulated would give that image, not that the simulated structure matches that of the interface. The models provided by the Z-contrast/EELS technique should therefore be viewed as accurate starting models for incorporation into more rigorous theoretical modelling techniques as well as for assisting in the interpretation of other microscopical results.

The sensitivity of the technique to subtle changes in bonding and structure as well as to segregants and interphases makes it ideal for characterizing the whole range of internal interfaces. For the clean homophase [001] tilt boundaries in $SrTiO_3$ studied here, the presence of half occupied atomic columns was found in all experimentally observed structures. Using the structural units from these results, grain boundary structures for the whole range (0–90°) of symmetric, asymmetric and mixed structure boundaries could be derived. The half columns in these structures represent a solution to the problem of like-ion repulsion that occurs in ionic grain boundaries and offer potential sites for the incorporation of dopants. Although the technique is not sensitive to the occurrence of individual vacancies in the pure structure, it will be sensitive to the presence of dopants at the grain boundary. Future work will investigate the effect of incorporating the dopants which give rise to the interesting properties of these materials into the boundary structure.

Acknowledgments

Various aspects of this research were performed in collaboration with V P Dravid, V Ravikumar, M M McGibbon, M F Chisholm and A J McGibbon. We would like to thank T C Estes and J T Luck for technical assistance. This research was sponsored by the Division of Materials Sciences, USA Department of Energy, under contract DE-AC05-84OR21400 with Martin Marietta Energy Systems, Inc and in part by an appointment to the Oak Ridge National Laboratory Postdoctoral Research Program administered by the Oak Ridge Institute for Science and Education.

References

[1] Merkle K L and Smith D J 1987 *Phys. Rev. Lett.* **59** 2887
[2] Ichinose H and Ishida Y 1981 *Phil. Mag.* A **43** 1253
[3] Trumble K P and Rühle M 1991 *Acta Metall. Mater.* **39** 1915–24
[4] Morrissey K J and Carter C B 1984 *J. Am. Ceram. Soc.* **67** 292
[5] Chisholm M F, Pennycook S J, Jebasinski R and Mantl S 1994 *Appl. Phys. Lett.* **64** 2409
[6] Jesson D E and Pennycook S J 1991 *Phys. Rev. Lett.* **66** 750
[7] Muller D A, Tzou Y, Raj R and Silcox J 1993 *Nature* **366** 725
[8] Mayer J 1992 *Proc. 50th Annual Proc. Microscopy Society of America* ed G W Bailey *et al* (San Francisco: San Francisco Press) pp 1198–9
[9] Hunt J A and Williams D B 1991 *Ultramicroscopy* **38** 47–73
[10] Jeanguillaume C and Colliex C 1988 *Ultramicroscopy* **28** 252–7
[11] McMullan D, Rodenburg J M, Murooka Y and McGibbon A J 1990 *Inst. Phys. Conf. Ser.* **98** 55–8
[12] Gubbens A J and Krivanek O L 1993 *Ultramicroscopy* **51** 146–59
[13] Browning N D, Chisholm M F and Pennycook S J 1993 *Nature* **366** 143–6
[14] Batson P E 1993 *Nature* **366** 727
[15] Muller D A, Subramian S, Sass S L, Silcox J and Batson P E 1994 *Proc. 13th Int. Congress on Electron Microscopy, Paris, 17–22 July* ed B Jouffrey and C Colliex (Paris: Editions de Physique) p 729
[16] Bruley J 1992 *Phil. Mag. Lett.* **66** 47
[17] Gatts C, Müllejans H, Bruley J and Rühle M 1994 *Proc. ICEM 94* ed B Jouffrey and C Colliex (Paris: Editions de Physique) p 745
[18] Brydson R, Müllejans H, Bruley J, Trusty P, Sun X, Yeomans J and Rühle M 1995 *J. Microsc.* **177** 369
[19] Kleebe H J, Bruley J and Rühle M 1994 *J. Eur. Ceram. Soc.* **14** 1
[20] Altermatt D and Brown I D 1985 *Acta Crystallogr.* B **41** 240
[21] Brown I D and Altermatt D 1985 *Acta Crystallogr.* B **41** 244

[22] Sutton A P and Vitek V 1983 *Phil. Trans. R. Soc. Lond.* A **309** 1
[23] Sutton A P 1988 *Acta Metall.* **36** 1291
[24] Fertig J and Rose H 1981 *Optik* **59** 407–29
[25] Loane R F, Kirkland E J and Silcox J 1988 *Acta Crystallogr.* A **44** 912–27
[26] Kirkland E J, Loane R F and Silcox J 1987 *Ultramicroscopy* **23** 77–96
[27] Loane R F, Xu P and Silcox J 1992 *Ultramicroscopy* **40** 121–38
[28] Pennycook S J and Jesson D E 1990 *Phys. Rev. Lett.* **64** 938–41
[29] Pennycook S J and Jesson D E 1992 *Acta Metall. Mater.* **40** S149–59
[30] Hall C R and Hirsch P B 1965 *Proc. R. Soc. Lond.* A **286** 158–77
[31] Bird D M and King Q A 1990 *Acta Crystallogr.* A **46** 202–8
[32] Warren B E 1990 *X-ray Diffraction* (New York: Dover)
[33] Jesson D E and Pennycook S J 1995 *Proc. R. Soc. Lond.* A **449** 273
[34] Gull S F and Daniell G J 1978 *Nature* **272** 686
[35] Gull S F and Skilling J 1984 *Proc. IEE* F **131** 646
[36] McGibbon A J, Jesson D E and Pennycook S J 1996 *J. Microsc.* at press
[37] McGibbon M M, Browning N D, Chisholm M F, McGibbon A J, Pennycook S J, Ravikumar V and Dravid V P 1994 *Science* **266** 102–5
[38] Egerton R F 1986 *Electron Energy Loss Spectroscopy in The Electron Microscope* (New York: Plenum)
[39] Grunes L A, Leapman R D, Wilker C N, Hoffman R and Kunz A B 1982 *Phys. Rev.* B **25** 7157
[40] Paterson J H and Krivanek O L 1990 *Ultramicroscopy* **32** 319
[41] Brydson R, Sauer H and Engel W 1992 *Transmission Electron Energy Loss Spectrometry in Materials Science* ed M M Disko, C C Ahn and B Fultz (Warrendale, PA: TMS Monograph Series)
[42] Pearson D H, Ahn C C and Fultz B 1993 *Phys. Rev.* B **47** 8471
[43] Ritchie R H and Howie A 1988 *Phil. Mag.* **58** 753–67
[44] Pennycook S J, Jesson D E and Browning N D 1995 *Nucl. Instrum. Methods* B **96** 575–82
[45] Browning N D and Pennycook S J 1995 *J. Microsc.* **180** 230–8
[46] Pennycook S J and Jesson D E 1996 *Handbook of Microscopy* ed S Amelinckx *et al* (Weinheim: VCH) at press
[47] Maslen V W and Rossouw C J 1983 *Phil Mag* A **47** 119–30
[48] Maslen V W and Rossouw C J 1984 *Phil Mag* A **49** 735–42
[49] Rossouw C J 1983 and Maslen V W 1984 *Phil Mag* A **49** 743–57
[50] Allen L J 1993 *Ultramicroscopy* **48** 97–106
[51] Allen L J and Rossouw C J 1990 *Phys. Rev.* B **42** 11644–54
[52] Holbrook O F and Bird D M 1995 *Proc. Microscopy and Microanalysis 1995, Proc. 53rd Ann. Meeting of the Microscopy Society of America* ed G W Bailey, M M Ellisman, R A Henniagar and N J Zaluzec, pp 278–9
[53] Taftø J and Krivanek O L 1982 *Nucl. Instrum. Methods* **194** 153
[54] Browning N D and Pennycook S J 1993 *Microbeam Analysis* **2** 81–9
[55] Pauling L 1929 *J. Am. Ceram. Soc.* **51** 1010
[56] Jansen L and Block R 1991 *Physica* C **181** 149
[57] FXL Solutions Ltd, 52 New Road, Ascot SL5 8QQ, UK
[58] Brydson R, Sauer H, Engel W and Hofer F 1992 *J. Phys.: Condens. Matter* **4** 3429
[59] McGibbon M M, Browning N D, Pennycook S J, Ravikumar V and Dravid V P 1994 *MRS Symp. Proc.* **319** 223
[60] Browning N D, Pennycook S J, Chisholm M F, McGibbon A J and McGibbon M M 1995 *Interface Sci.* **2** 397
[61] McGibbon M M, Browning N D, McGibbon A J and Pennycook S J 1996 *Phil. Mag.* at press
[62] Merkle K L and Wolf D 1992 *Phil. Mag.* A **65** 513
[63] Merkle K L 1992 *Ultramicroscopy* **40** 281
[64] Read W T and Shockley W 1950 *Phys. Rev.* **78** 275
[65] King A H and Smith D A 1980 *Acta Crystallogr.* A **36** 335
[66] Hirth J P and Lothe J 1982 *Theory of Dislocations* (New York: Wiley)
[67] Rice R W 1966 *Materials Science Research* vol 3, ed W W Kriegel and H Palmour III (New York: Plenum) p 387
[68] Balluffi R W, Bristowe P D and Sun C P 1981 *J. Am. Ceram. Soc.* **64** 23
[69] Fonda R W and Luzzi D E 1993 *Phil. Mag.* A **68** 1151
[70] Yamaoka N, Masuyama M and Fukui M 1983 *Ceramic Bulletin* **62** 698
[71] Rossinelli M, Greuter F and Schmükle F 1989 *Br. Ceram. Proc.: Electroceram.* **41** 177
[72] Stucki F and Greuter F 1990 *Appl. Phys. Lett.* **57** 446
[73] Gaucher P, Perrier R L and Ganne J P 1988 *Adv. Ceram. Mater.* **3** 273
[74] Ravikumar V and Dravid V P 1996 *J. Phys. D: Appl. Phys.* **29** 1799
[75] Chiang Y-M and Takagi T 1990 *J. Am. Ceram. Soc.* **73** 3278
[76] Chiang Y-M and Takagi T 1990 *J. Am. Ceram. Soc.* **73** 3286
[77] Desu S B and Payne D A 1990 *J. Am. Ceram. Soc.* **73** 3398
[78] Desu S B and Payne D A 1990 *J. Am. Ceram. Soc.* **73** 3407
[79] Fujimoto M and Kingery W D 1985 *J. Am. Ceram. Soc.* **68** 169